Acta Crystallographica Section A
**Foundations of Crystallography**
ISSN 0108-7673

Received 5 July 2011
Accepted 6 June 2012

# Short-range order in multicomponent materials

**Anna V. Ceguerra,[a,b]* Michael P. Moody,[c] Rebecca C. Powles,[a] Timothy C. Petersen,[d] Ross K. W. Marceau[e] and Simon P. Ringer[a,b,f]***

[a]School of Aerospace, Mechanical and Mechatronic Engineering, The University of Sydney, Australia, [b]Australian Centre for Microscopy & Microanalysis, The University of Sydney, NSW 2006, Australia, [c]Department of Materials, University of Oxford, Parks Road, Oxford OX1 3PH, UK, [d]School of Physics, Monash University, Victoria 3800, Australia, [e]Max-Planck Institut für Eisenforschung, Max-Planck-Str. 1, D-40237 Düsseldorf, Germany, and [f]ARC Centre of Excellence for Design in Light Metals, Australia. Correspondence e-mail: anna.ceguerra@sydney.edu.au, simon.ringer@sydney.edu.au

The generalized multicomponent short-range order (GM-SRO) parameter has been adapted for the characterization of short-range order within the highly chemically and spatially resolved three-dimensional atomistic images provided by the microscopy technique of atom-probe tomography (APT). It is demonstrated that, despite the experimental limitations of APT, in many cases the GM-SRO results derived from APT data can provide a highly representative description of the atomic scale chemical arrangement in the original specimen. Further, based upon a target set of the GM-SRO parameters, measured from APT experiments, a Monte Carlo algorithm was utilized to simulate statistically equivalent atomistic systems which, unlike APT data, are complete and lattice based. The simulations replicate solute structures that are statistically consistent with other correlation measures such as solute cluster distributions, enable more quantitative characterization of nanostructural phenomena in the original specimen and, significantly, can be incorporated directly into other models and simulations.



## 1. Introduction

There is considerable interest in the study of the atomic scale architecture of solute and dopant atoms within a growing range of technologically important materials systems. In many materials the distribution of nanoscale atomic clusters that can form during the very early stages of elevated temperature ageing dictate the nucleation pathways for precipitation (Ringer & Hono, 2000; Nie *et al.*, 2002; Clouet *et al.*, 2006). Furthermore, there is an increasing consensus that clusters themselves exert significant influence on bulk material properties and performance (Castell *et al.*, 2003; Heinrich *et al.*, 2003; Pereloma *et al.*, 2004; Ralston *et al.*, 2010; Marceau *et al.*, 2010). However, much still remains to be understood about these phenomena. This is due largely to experimental limitations in the determination of chemistry and three-dimensional structure at the nanoscale. Moreover, at the atomic scale there is an inherent complexity in describing the intricate nature of chemical distribution throughout the crystal in multicomponent materials.

To this end, in 1950 Cowley presented a new definition of short-range order (SRO) to describe the solute distribution within a binary alloy (Cowley, 1950*b*). This definition, known widely as the Warren–Cowley (WC) SRO parameter, was later extended by de Fontaine to describe pairwise correlations in multicomponent systems (de Fontaine, 1971). Recently, Ceguerra *et al.* developed a comprehensive generalized multicomponent (GM) SRO formalism, using the expression introduced by Cowley, which allows a more complete description of solute arrangements in complex solid solutions (Ceguerra, Powles *et al.*, 2010). SRO is a powerful measure of the relationships between atomic species and is a robust method for investigating solute clustering phenomena. However, its true potential thus far has been constrained by experimental limitations.

Conventionally, SRO parameters are measured from the analysis of diffuse scattering in X-ray diffraction patterns from, most usually, binary systems (Cowley, 1950*a*; Welberry, 1985). These concise measures of pair correlations arise naturally from kinematical diffraction physics and it can be shown that the SRO parameters are proportional to the peak heights of the Patterson function: a generalized form of radial distribution function (Cowley, 1960). SRO analysis of the diffraction patterns involves identifying and separating the intensities due to diffuse scattering which, in part, are generated by disorder in the occupation of crystal lattice sites by different elemental species. Other phenomena besides this chemical disorder may give rise to diffuse scattering, and this complicates interpretation. Structural disorder in the form of deviations from the perfect lattice can arise as a result of 'size

effects' or perturbations of atomic positions caused by atomic interactions, and these serve to displace the diffuse peaks. For binary alloys under the kinematical approximation, Cowley derived expressions to accommodate such effects (Cowley, 1968), which remedy the interpretation issue. Cowley & Murray (1968) also extended the SRO parameters by including higher-order correlation functions to account for departures from single scattering approximations, as can occur for dynamical interactions in electron diffraction. Higher-order correlations also arise from the size effects, although these can be neglected if the displacements are small, but the general interpretation is quite complicated (Cowley, 1995). Clearly, all of these considerations become considerably more complex for ternary or multicomponent alloys. For example, in a multicomponent system containing $n$ different elements, $n(n-1)/2$ distinct radiations are required in order to resolve the pairwise SRO signals from diffuse scattering experiments (de Fontaine, 1971).

Interpretation issues for diffuse scattering by SRO can be overcome by simulating diffraction patterns from hypothesized atomic configurations and comparing with experiment. For modelling SRO in non-crystalline materials, McGreevy & Pusztai (1988) developed a reverse Monte Carlo (RMC) algorithm, which produces ensembles of atomic configurations made consistent with experiment by iteratively minimizing the difference between simulated and experimental diffraction data. The RMC method provides an interpretation of pair-correlated diffuse scattering from disordered structures such as glasses. The algorithm has been extended to model disordered crystals (Nield *et al.*, 1992) and single crystals to describe diffuse scattering in conjunction with sharp Bragg diffraction (Nield *et al.*, 1995). Proffen & Welberry (1997) explicitly considered occupational and displacement disorder and prescribed refinements to the algorithm, required for systems containing both of these scattering contributions. The computationally intensive nature of RMC modelling of SRO for single crystals was later emphasized (Proffen & Welberry, 1998; Welberry & Proffen, 1998), whilst Tucker *et al.* (2001) espoused the benefits of polycrystalline specimens to concurrently model diffuse and Bragg scattering in an efficient manner. The RMC method has also been applied to model diffuse scattering from magnetic SRO in neutron powder diffraction (Mellergård & McGreevy, 1999).

Alternatively, the quantification of the multicomponent SRO is well suited to the real-space three-dimensional atomistic reconstructions generated in atom-probe tomography (APT). The extremely high chemical and spatial resolution analyses provided in APT enable the direct microscopic imaging of atomic clusters which can represent a subtle, but significant, local chemistry perturbation that may contain just a few atoms in a solid solution. This distinguishes APT from many other techniques, because it provides *direct* three-dimensional chemical information on this length scale, whereas other microscopies cannot achieve the combined levels of chemical and spatial resolution required for such measurements. APT eliminates the substantial effort of measuring the GM-SRO using diffuse scattering experiments. In fact, the pairwise nature of diffraction studies would have limited the capacity of each GM-SRO in incorporating an unlimited number of elements. Instead, APT provides the means to characterize such complex correlations through the model of crystallographic shells in real space. This was achieved through the development of an approach for characterizing the GM-SRO parameters as a function of atomic radial distances.

However, APT is constrained by certain limitations which can affect its capacity to measure SRO. The first is the finite detection efficiency of the instrument itself resulting in the stochastic exclusion of at least ~43% of all atoms from the final three-dimensional reconstruction. Another significant issue is limited spatial resolution which blurs the positions of the atoms from their true lattice sites, resulting in the partial or full loss of the crystalline atomic structure. The quantification of these issues has been the subject of detailed analyses and modelling (Geiser *et al.*, 2007; Cadel *et al.*, 2009; Moody *et al.*, 2009; Gault, Moody *et al.*, 2010). Given the highly resolved atomic information available from the atom probe and the nature of the above experimental limitations in scattering, we have investigated the viability of characterizing solute SRO using this atomistic microscopy technique.

## 2. Theory

### 2.1. GM-SRO parameter

The GM-SRO parameter (Ceguerra, Powles *et al.*, 2010) is a definition used to describe the chemical short-range order of a multicomponent system. It has its basis in the WC-SRO parameter (Cowley, 1950*b*)

$$\alpha_{BA}^{m} = \frac{(p_{BA}^{m} - X_A)}{(1 - X_A)}, \tag{1}$$

where in a binary system with composition $X_A$, $p_{BA}^{m}$ is the probability of finding an $A$ atom in the $m$th crystallographic shell around a $B$ atom. Fig. 1(*a*) is a simple illustration of how the SRO analysis interrogates the local atomic neighbourhood based upon the well defined shell structure of a perfect lattice. The WC-SRO expression was later extended by de Fontaine who derived a theoretical pairwise multicomponent SRO (PM-SRO) parameter (de Fontaine, 1971) suitable for the characterization of more complicated materials. In a ternary $A$–$B$–$C$ system, the PM-SRO is calculated by considering the pairwise probabilities of finding an atom of type $C$ around another atom of type $B$:

$$\alpha_{BC}^{m} = \frac{(p_{BC}^{m} - X_C)}{(\delta_{BC} - X_C)}. \tag{2}$$

From the perspective of kinematic diffraction, which accounts for pair correlations only and not triplets/quadruplets/multiplets *etc.*, the PM-SRO provides an adequate generalization of the original WC-SRO parameters. Despite the fact that pair correlations contain much structural and chemical information, and that these are currently used as the predominant quantitative descriptors of short-range ordering from

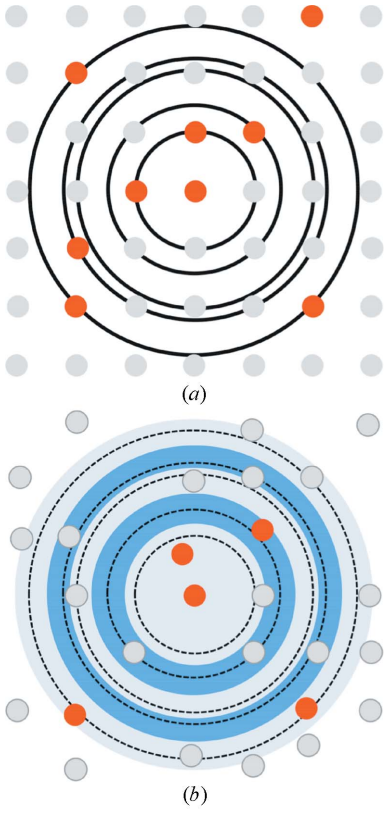


**Figure 1**
Schematic of the definition of atomic shells for the GM-SRO calculation. (*a*) A perfect crystal lattice in which atoms are separated by discrete radii and hence shells are easily defined. (*b*) A two-dimensional illustration of atom-probe data with finite detection efficiency and spatial resolution effects. Atoms from the same shell can no longer be exactly defined by a single radius from the central atom. Instead shells are defined by a finite width as illustrated by the shading. Atoms occurring within a certain shaded region are assigned to the respective shell.

reciprocal-space data, modern atom-probe data sets can provide the real-space positions and *chemical* identities of around 100 million atoms in three dimensions. This therefore offers the potential for a richer short-range order descriptor to account for multicomponent correlations and offers a convenient means to statistically reduce the vast complexity of structural and compositional correlations that exist in such data sets. Structural correlations beyond pairs can be readily computed from atom-probe data, such as triplet distribution functions and so on.

The GM-SRO parameter equation [equation (3)] further extends the definition of SRO for the consideration of ternary or higher-order multicomponent correlations. The expression for the GM-SRO is generalized from the PM-SRO definition, which is also amenable to shell-based correlations, but unlike the GM-SRO it only correlates *pairs of elements* in multicomponent systems, and it does not consider *multicomponent correlations* (*i.e.* between sets of elements). The GM-SRO parameters are defined in terms of *structural pair correlations* by retaining the concept of neighbour shells and are generalized to include higher-order *compositional correlations*, but similar to the PM-SRO they do not provide higher-order structural correlations (such as triplets, which contain information about bond angles *etc*). They do, however, contain significant crystallographic information by virtue of the shell distances – for instance, in face-centred cubic (f.c.c.) crystals the first shell contains neighbouring atoms that are ⟨110⟩ family of directions from the centre atom, the second shell is ⟨100⟩. In principle, higher-order structural correlations could also be incorporated by dispensing with shells; however, this would add significant complexity and the statistical utility of such information may be called into question.

**Table 1**
Number of PM-SRO and GM-SRO parameters according to the number of components in the system.

| Components | No. of PM-SRO parameters | No. of GM-SRO parameters |
|---|---|---|
| 2 | 4 | 9 |
| 3 | 9 | 49 |
| 4 | 16 | 225 |
| 5 | 25 | 961 |
| 6 | 36 | 3969 |
| 7 | 49 | 16129 |
| 8 | 64 | 65025 |
| 9 | 81 | 261121 |
| 10 | 100 | 1046529 |
| 11 | 121 | 4190209 |

The GM-SRO parameter is defined as

$$\alpha^{m}_{\{B_j\}_{j=1}^{k}\{C_l\}_{l=1}^{h}} = (-1)^{\left(1+\delta_{\{B_j\}_{j=1}^{k}\{C_l\}_{l=1}^{h}}\right)}\left(\frac{p^{m}_{\{B_j\}_{j=1}^{k}\{C_l\}_{l=1}^{h}} - X_{\{C_l\}_{l=1}^{h}}}{\delta_{\{B_j\}_{j=1}^{k}\{C_l\}_{l=1}^{h}} - X_{\{C_l\}_{l=1}^{h}}}\right), \tag{3}$$

where $p^{m}_{\{B_j\}_{j=1}^{k}\{C_l\}_{l=1}^{h}}$ represents the probability that in the $m$th crystallographic shell around any atom belonging to the set of $k$ different elements $\{B_j\}$ there occurs an atom belonging to a second set of $h$ different elements $\{C_l\}$, which may or may not overlap with $\{B_j\}$. This probability is defined as

$$p^{m}_{\{B_j\}_{j=1}^{k}\{C_l\}_{l=1}^{h}} = \frac{\sum_{j=1}^{k}\left[N_{B_j}\sum_{l=1}^{h}p^{m}_{B_jC_l}\right]}{\sum_{j=1}^{k}N_{B_j}}, \tag{4}$$

where $N_{B_j}$ is the number of atoms of type $B_j$. The leading term in the GM-SRO definition [equation (3)] is incorporated only to simplify interpretation of the results. It is needed for those cases when $\delta_{\{B_j\}_{j=1}^{k}\{C_l\}_{l=1}^{h}} = 0$, and its only function is to ensure a positive value of a GM-SRO parameter is indicative of co-segregation at that crystallographic shell, whereas a negative value indicates anti-segregation of the two sets of elements. The generality of the GM-SRO arises from its ability to consider the correlation existing between two sets of elements within a single parameter. In the case where the characterization of chemical–spatial relationships between two sets of elements is of interest, the GM-SRO provides the capacity to manage the complexity of multicomponent correlations. The number of GM-SRO parameters is equal to the total number of all possible combinations of possible sets of elements $\{B_j\}$ and $\{C_l\}$. Table 1 shows a comparison for the total number of GM-SRO parameters *versus* PM-SRO for describing possible

correlations in a material system as a function of the number of components it contains.

### 2.2. Application of GM-SRO to atom-probe data

In APT, single atoms are successively removed from the surface of a very sharp needle-shaped specimen by field evaporation (Kelly & Miller, 2007; Seidman, 2007). The diverging electric field at the apex of the specimen gives rise to a highly magnified projection of the ions onto a position-sensitive detector at some distance from the specimen. To characterize ionic identity by time-of-flight mass spectrometry, an electric field is generated by the superimposition of a DC voltage and a high-voltage (HV) pulse. Alternatively, the HV pulse can be replaced with ultra-short laser pulses to generate ionization events. Each hit on the detector can be directly related to the pulse responsible for the corresponding ionization event, facilitating highly accurate time-of-flight measurements and mass resolution. A reverse-projection algorithm, combined with the sequence of evaporation and an assumed model for specimen shape, enables a three-dimensional atomistic reconstruction of the analysed volume (Bas *et al.*, 1995; Gault *et al.*, 2011). These reconstructions contain a considerable amount of information, routinely incorporating in the range of $10^7$–$10^9$ atoms, and providing an excellent statistical basis for analysing the spatial distribution of solutes within the localized volume of interest.

The spatial resolution of APT is extremely high (Cadel *et al.*, 2009; Gault *et al.*, 2009; Gault, Moody *et al.*, 2010). However typical interatomic spacings are smaller than the lateral resolution, resulting in the loss of significant crystallographic information. The blurring of the lattice in the reconstruction is due to a combination of trajectory aberrations in the flight path of the ions, local geometric and compositional variations on the surface of the specimen, and the simplified model of the evaporation geometry utilized in the three-dimensional reconstruction. Further, there is a random loss in detection efficiency due to the limited open area of the micro-channel plate (MCP) detectors, and ~43% of the atoms evaporated from the specimen are consequently lost from the final analysis. This is a design limitation common to all current atom-probe detectors. However, despite their exclusion from the data, the undetected atoms are taken into consideration in the creation of the tomographic reconstruction, meaning that high-precision interatomic distances between the detected atoms are still achieved. Ultimately, the limited lateral resolution and detector efficiency prevent the direct analysis of crystallographic structure from current atom-probe data sets.

The application of GM-SRO measurements has previously been demonstrated for the characterization of simulations, in which atoms are constrained to a perfect three-dimensional lattice configuration of atoms (Ceguerra, Powles *et al.*, 2010). In such a system all the atoms neighbouring a reference atom can be thought of as being arranged in shells at discrete radii, as illustrated in Fig. 1(*a*). With knowledge of the type of crystal and the theoretical lattice parameter of the system, these radii can be predicted. In a perfect crystalline system the shell may be considered as an infinitely thin theoretical surface. However, APT data are imperfect. As illustrated in Fig. 1(*b*), a significant fraction of atoms are missing from the system in the local neighbourhood surrounding each atom, because of the limited detection efficiency of the experiment. Furthermore, those atoms that are measured are slightly offset from their true lattice positions.

The GM-SRO calculation must be specifically adapted for the application to experimental APT data. Hence, the definition of the atomic shells has been adapted such that it now incorporates a finite width, indicated by the shading in Fig. 1(*b*). The extent of the $m$th shell thickness is determined by the theoretical perfect crystal $(m-1)$th, $m$th and $(m+1)$th shell surface radii, which are $r_{m-1}$, $r_m$ and $r_{m+1}$, respectively. Consequently atom $j$ is defined to be an $m$th shell neighbour of atom $i$ if they are separated by a distance $d_{ij}$ such that

$$\frac{r_{m-1}+r_m}{2} < d_{ij} < \frac{r_m+r_{m+1}}{2}. \qquad (5)$$

This enables the characterization of imperfect systems *via* a shell-based GM-SRO analysis. The integration of pair correlations within shells mimics the same procedure used to quantitatively estimate coordination numbers for radial distribution functions of structurally disordered solids (Cockayne & McKenzie, 1988).

### 2.3. Monte Carlo simulations based on target GM-SRO

Complementary experimental methods for measuring SRO, such as CALPHAD (calculation of phase diagrams) and X-ray diffraction, have an advantage in that the exact atomic positions and identities are not required (Cowley, 1950*b*; Zhu *et al.*, 2004). However, a significant disadvantage of these approaches is that the three-dimensional atomic structure cannot be explored in finer detail. Monte Carlo (MC) simulation approaches have previously been developed to recreate an atomic scale system with statistically equivalent SRO (Gehlen & Cohen, 1965; Gerold & Kern, 1987). In these simulations, the acceptance or rejection of trial moves is based on their effect upon the overall SRO of the system, rather than the more usual approach of comparing potential energies, such as in the Metropolis algorithm (Newman & Barkema, 1999).

The goal of the MC simulations here is to drive the system towards an atomic configuration with a particular, predefined GM-SRO. In this case, defining whether or not the swapping of a pair of atoms has improved the overall configuration of the system is not straightforward. The target SRO consists of a set of GM-SRO parameters. For example, take the case of an $A$–$B$–$C$ ternary alloy, with a target subset of GM-SRO $\{\alpha_{AA}, \alpha_{AB}, \alpha_{AC}, \alpha_{BA}, \ldots, \alpha_{CB}, \alpha_{CC}\}$ defined for the $m = 1$ shell. It is possible that the action of randomly swapping a pair of atoms may move the system towards the $\alpha_{BA}$ target but simultaneously also move the system away from the $\alpha_{CB}$ target. Hence some objective metric is required in the algorithm to decide on whether the trial move has either improved or worsened the overall atom configuration of the simulated system. To this end a 'residual' can be defined, as a measure of

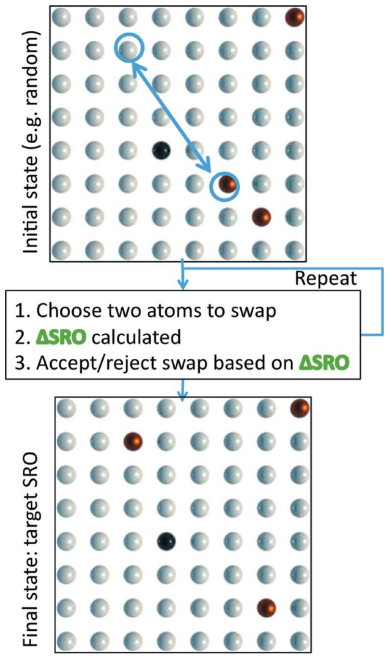


**Figure 2**
Monte Carlo algorithm schematic. From an initial configuration, the following steps are repeated until a chemical configuration is reached that satisfies the target SRO conditions: (i) choose two dissimilar atoms to swap, (ii) calculate the change in SRO, and (iii) accept the swap if the difference between the current SRO and the target SRO has reduced.

the difference in the current SRO order of the system, denoted by '$t$' in $\{\alpha^t_{AA}, \alpha^t_{AB}, \alpha^t_{AC}, \alpha^t_{BA}, \ldots, \alpha^t_{CB}, \alpha^t_{CC}\}$, and the target SRO $\{\alpha_{AA}, \alpha_{AB}, \alpha_{AC}, \alpha_{BA}, \ldots, \alpha_{CB}, \alpha_{CC}\}$. There are various ways to define the residual (Gehlen & Cohen, 1965; Gerold & Kern, 1987); however, the precise nature of the selected definition is critical, since it is central to the efficiency of the MC algorithm, and influences the capability of the MC method to achieve a system configuration with the target GM-SRO. For the purposes of this study, the residual was defined by

$$\Delta_{\mathrm{GM-SRO}} = \sum |\alpha_{ij} - \alpha^t_{ij}|. \qquad (6)$$

This residual is then used to accept or reject steps within the algorithm. The fundamental approach of our algorithm, illustrated in Fig. 2, is as follows:

(i) Determine a pair of atoms for trial move.
(ii) Swap atom positions.
(iii) Calculate overall GM-SRO residual due to trial move.
(iv) If the GM-SRO residual is decreased:
(*a*) move is accepted.
(v) If the GM-SRO residual is increased:
(*a*) move is accepted with random probability, or
(*b*) move is rejected and atoms are swapped back to original positions.
(vi) Repeat until reaching target GM-SRO or after $n$ successive moves fail to decrease residual.

The required number of trial moves is dependent on the magnitude of the difference between the target and the current GM-SRO parameter values, the concentration of each element, the number of shells, the size of the data set and the number of components.

Several computational enhancements were made to improve the efficiency of the algorithm. Firstly, a $k$-dimensional tree data structure (Bentley, 1975) was applied to the analysis, providing excellent performance in searching for the $k$ nearest neighbours around each reference atom and enabling efficient recalculation of the GM-SRO at each step in the simulation. This structure is also memory efficient. Next, only the change in GM-SRO due to each trial move was calculated, rather than recalculating the entire set of GM-SRO parameters at each step. Further, selection of the atoms for the trial swap was not completely random but based in part upon the chemical identity of the atoms and the potential that randomly moving atoms of this kind would decrease the residual between a specific GM-SRO's target and current values. The combination of these enhancements enables simulation cells as large as 32 million atoms – or even higher – to reach the target GM-SRO parameters within $\sim 10^9$ steps for multiple shells. These system sizes are commensurate with modern APT data sets obtained from experiments and are plausible on a medium-performance computational platform.

### 2.4. Simulations investigating the validity of GM-SRO measurements *via* APT

Short-range order is one way to describe the detailed nature of the atomic scale chemical distributions in any given crystal system. Hence, solute clustering is inextricably linked to the GM-SRO measured in the system. This is demonstrated in Fig. 3. Simulated systems were generated for a simple binary alloy containing 1 million atoms, for compositions of solute element $B$ as $X_B = 0.1$, 1.0 and 5.0 (at.%), respectively, and for the target GM-SRO parameter $\alpha^{m=1}_{BB} = 0$ (equivalent to a random solute dispersion), 0.001 and 0.01, respectively, *via* the MC approach described above, on an f.c.c. crystal with a lattice parameter of 0.404 nm. The cluster-size frequency distributions within the resulting simulated systems were measured *via* the three-dimensional Markov field (3DMF) algorithm (Ceguerra, Moody *et al.*, 2010). This definition of clustering is based upon the definition that two solutes are clustered if they are first-shell ($m = 1$) nearest neighbours. Thus, Fig. 3 demonstrates the particular way that the cluster-size distribution changes to incorporate increasingly large clusters, as $X_B$ and/or $\alpha^{m=1}_{BB}$ increase.

In the next step the perfect lattice systems generated by the MC simulations were modified to account for limitations in atom-probe detector efficiency and spatial resolution. By incorporating these experimental effects, we can approximate how APT would image the original simulations and thereby begin to address a key question: how well do APT-derived GM-SRO measurements represent the actual values of the original system?

The atom-probe detector efficiency was simulated simply by the stochastic removal of a specific fraction of atoms from the perfect f.c.c. crystal with a lattice parameter of 0.404 nm. For example, in order to simulate the effect of 90% detection

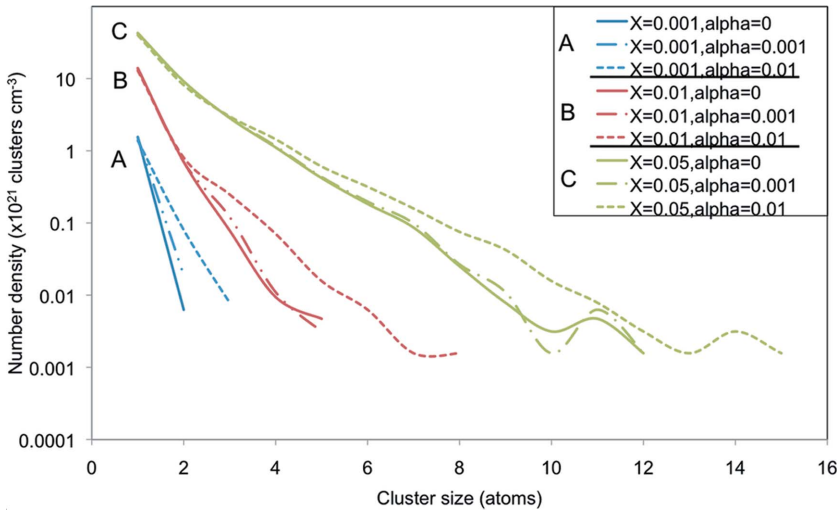


**Figure 3**
Cluster-size distribution of a model binary system as represented by the number density of clusters (per $cm^3$) *versus* cluster size (in atoms), as a function of both concentration of the minor element $X$ and GM-SRO. Each series ($A$, $B$ and $C$) contains a specific solute concentration, and is divided into three plots comprised of an SRO of 0, 0.001 and 0.01. Series $A$ describes a system with 0.001 (0.1%) solute concentration; series $B$ is a system with 0.01 (1%) solute concentration; and series $C$ contains 0.05 (5%) solute. All are in at.%.

efficiency, 10% of the atoms in the simulation were randomly selected and removed. Limited spatial resolution, which effectively results in a blurring of the crystal, was modelled by applying a random offset to each atomic lattice position. The spatial resolution of APT is anisotropic, more precise in the in-depth direction ($z$) than laterally ($x$–$y$). Hence the size and direction of each random offset are individually determined by an ellipsoidal three-dimensional Gaussian probability distribution about each crystallographic point. Based upon previous investigations of APT resolution, the Gaussian was defined by a full width at half-maximum (FWHM) of 0.2 nm laterally and 0.06 nm in depth (Vurpillot *et al.*, 2004; Cadel *et al.*, 2009; Gault, La Fontaine *et al.*, 2010; Gault, Moody *et al.*, 2010). This approach has been adopted for a variety of previous APT investigations (Geiser *et al.*, 2007; Haley *et al.*, 2009; Moody *et al.*, 2009). However, it should be noted that these simple techniques to model the nature of atom-probe data are only approximate and cannot account for all the complexities in the field evaporation and subsequent reconstruction that contribute to the spatial resolution and detector efficiency. Nevertheless, this somewhat pragmatic approach is sufficient for the purposes of investigating the influence of these experimental limitations on the GM-SRO analysis.

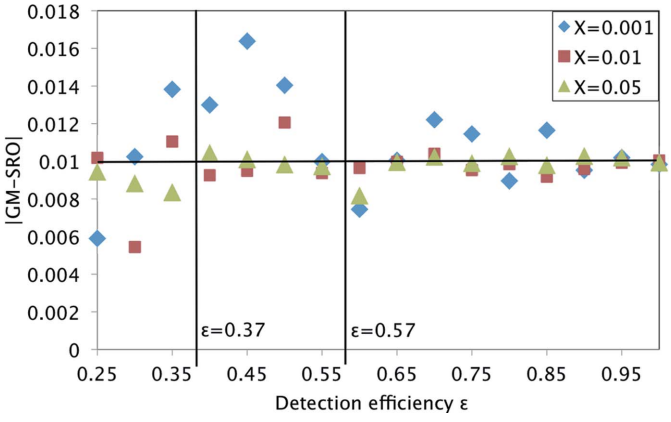


**Figure 4**
Effect of model detector efficiency on the first-shell GM-SRO (for solute–solute correlation) of three simulated binary data sets with approximately 1 million atoms, with solute concentrations of 0.001 (0.1%), 0.01 (1%) and 0.05 (5%) and the same theoretical GM-SRO of 0.01. Vertical lines indicate estimated detection efficiencies of a conventional straight ion flight path atom probe (0.57) and an atom probe fitted with a reflectron (0.37).

Fig. 4 plots the GM-SRO as a function of model detection efficiency, for three f.c.c. (lattice parameter = 0.404 nm) binary systems with solute concentrations of $X_B$ = 0.1, 1.0 and 5.0 at.%. In each case $\alpha_{BB}^{m=1}$ = 0.01 and the simulation comprised $10^6$ atoms. In the simulations with two higher solute concentrations the influence of decreasing detection efficiency is negligible even down to values of ∼40%. However, at low detection efficiencies, the spread of values of $\alpha_{BB}^{m=1}$ quickly increases. This is due to the statistical uncertainty introduced by the removal of larger numbers of atoms. This uncertainty is accentuated as the alloy compositions become more dilute, resulting in a higher degree of divergence from the target value of $\alpha_{BB}^{m=1}$ = 0.01, for the lowest values of $X_B$. This can be explained by the lower number of solute atoms in the simulation available to contribute to the GM-SRO measurement. For $X_B$ = 0.1 at.% simulation, there are only 1000 solute atoms in a complete data set, and with a detection efficiency of 0.57, for example, there are only 570 atoms.

Fig. 5 plots the solute–solute GM-SRO as a function of the FWHM of a spherical Gaussian probability distribution applied to randomly displace each atom from the perfect f.c.c. crystal (lattice parameter 0.404 nm, $X_B$ = 1.0 at.%). In this case, a spherical Gaussian was implemented instead of an

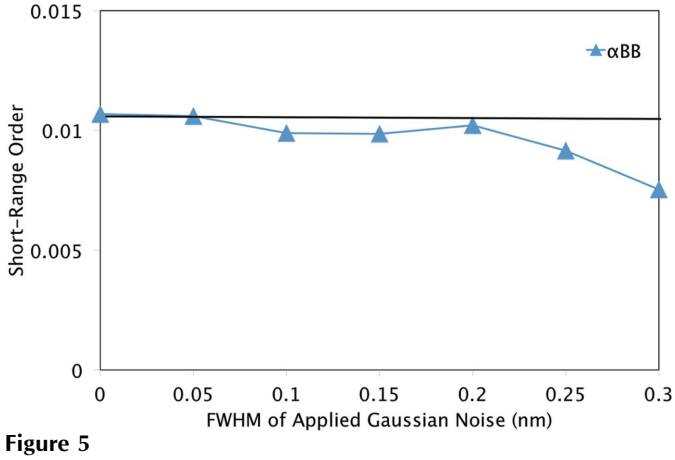


**Figure 5**
Effect of spherical Gaussian noise on first-shell GM-SRO, on an atomistic system with solute–solute GM-SRO = 0.01, $X_B$ = 1.0 at.% and efficiency level at 0.57.

ellipsoidal Gaussian for simplicity in interpreting the results. In actuality, a spherical Gaussian will tend to overestimate the spatial blurring of the lattice. Here, an *A*–*B* binary system with a GM-SRO value of $\alpha_{BB}^{m=1}$ ~0.01 and a detector efficiency of 57% was simulated. Fig. 5 demonstrates that, for this example, spatial blurring with FWHM values below ~0.2 nm has a limited impact on the GM-SRO.

### 2.5. Recreating the solute distribution of the original system

In the next step theoretical investigations were undertaken to address another significant question: based upon GM-SRO measurements of incomplete, APT-like data, are MC simulations able to recreate a lattice-based atomistic distribution that is statistically equivalent to the perfect and complete original system?

The three perfect, simulated binary *A*–*B* systems with solute concentrations of $X_B$ = 0.1, 1.0 and 5.0 (at.%) and possessing a GM-SRO parameter of $\alpha_{BB}^{m=1}$ = 0.01, calculated for the analyses in Fig. 3, served as the basis of these calculations. Each system was subject to stochastic removal of 43% of the atoms and a spatial blurring of the atomic coordinates from their ideal lattice positions to model an APT analysis. The 3DMF cluster-characterization procedure was subsequently applied and cluster-size frequency distributions calculated. In a perfect Al-based lattice system, a distance of 0.286 nm would separate two clustered solutes. However, as illustrated in Fig. 1(*b*), in APT data (or APT-like simulated data), first-shell nearest neighbours are more difficult to identify. Hence in this study, solutes separated by a distance less than $d_{max}$ = 0.35 nm were identified as being clustered. This value of $d_{max}$ was chosen as a compromise between maximizing the inclusion of potential first-shell neighbours (theoretically occurring at 0.286 nm) and minimizing the inclusion of second-shell ($m$ = 2) nearest neighbours (0.404 nm). This represents only one possible definition of clustering within APT data, although various others have been developed (Hyde & English, 2000; Vaumousse *et al.*, 2003; Miller & Kenik, 2004; Stephenson *et al.*, 2007).

Fig. 6 provides a comparison between the original cluster-size distributions presented in Fig. 3 and the APT-limited distributions, derived by the above analysis. The effects of finite detection efficiency and limited spatial resolution are pronounced, leading to a distribution of less frequent and smaller solute clusters than in the original system. The solute–solute GM-SRO of these artificially deteriorated systems was then measured, and these values used as target inputs to the MC simulation so as to generate a new complete and lattice-based system. The 3DMF procedure was again used to characterize the cluster-size frequency distribution in the resulting simulations and the results are also presented in Fig. 6. There is excellent agreement between the cluster distributions resulting from the MC simulations and those from the original simulated systems.

Fig. 7 provides a summary of the approach used here, in a simple flow chart.

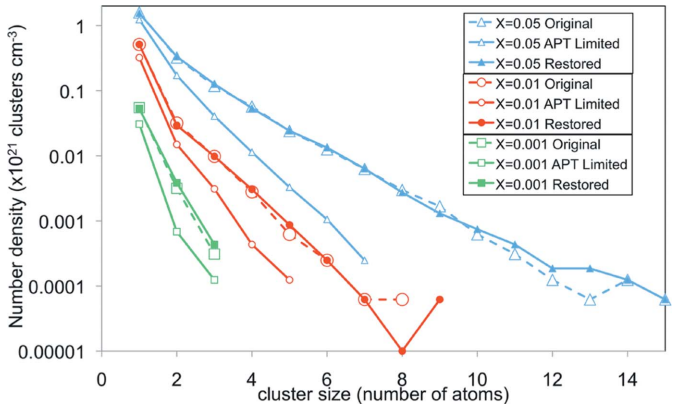


**Figure 6**
Number density of clusters (per cm$^3$) *versus* cluster size (in atoms), as a function of concentration ($X_B$ = 0.001, 0.05 and 0.01) in a simulated 1 million atom binary system, having initial GM-SRO = 0.01 (solute–solute).

(*a*) A perfect *A*–*B* lattice system with composition $X_B$ and GM-SRO = $\alpha_{BB}$ was generated *via* atomistic simulation using our MC methods.

(*b*) The cluster-size distributions were calculated using the 3DMF procedure.

(*c*) Typical aberrations found in atom-probe experiments were simulated by the spatial blurring of the atomic lattice and the random removal of 43% of all atoms. This accounts for APT spatial resolution and detector efficiency, respectively.

(*d*) The cluster-size distribution and GM-SRO = $\alpha_{BB}$* of these deteriorated (APT-like) systems were calculated using the same 3DMF procedures.

(*e*) A new atomistic simulation was generated using the MC approach based on the target GM-SRO = $\alpha_{BB}$* values derived from the deteriorated systems.

(*f*) The cluster-size distribution of these new systems was computed and compared to the original distribution.

The simulations indicate that even after deterioration of the simulation, akin to viewing a specimen through the lens of APT, there can remain enough crystallographic information to estimate the atomic scale solute distribution in the original system. This approach is now applied to actual APT data.

## 3. Atom-probe experiment

An Al–1.1 Cu–1.7 Mg (at.%) alloy was prepared by induction melting and direct casting into an ingot mould. The cast ingot was homogenized at 773 K for 16 h and water quenched. Afterwards, sample blanks were prepared and solution heat treated at 798 K for 1 h, quenched rapidly into cold water and then immediately aged at 423 K for 60 s in one case, and for 1 h in a second case. Specimens were prepared for atom-probe experiments using standard two-stage electropolishing techniques (Miller, 2000). Atom-probe specimens were analysed using a Cameca LEAP 3000X, equipped with a delay line detector. Experiments were conducted at a voltage pulse fraction of 0.25, with the specimen maintained at cryogenic temperatures (23 K) under ultra-high vacuum conditions (<4.5 $\times$ $10^{-9}$ Pa). A constant detection rate of 2 $\times$ $10^{-2}$ ions per

pulse was ensured by control on the total voltage applied to the tip.

Using the data acquired from these experiments, a three-dimensional reconstruction was generated using the commercial *IVAS* software, employing the advanced calibration technique outlined by Gault, Moody *et al.* (2010). Further data processing was performed, whereby the atoms occurring at the top and bottom tails of the 100th nearest-neighbour density distribution were removed as described in Stephenson *et al.* (2007). This procedure eliminates regions of aberrantly high and low atomic density, such as those usually associated with the presence of crystallographic poles within the data.

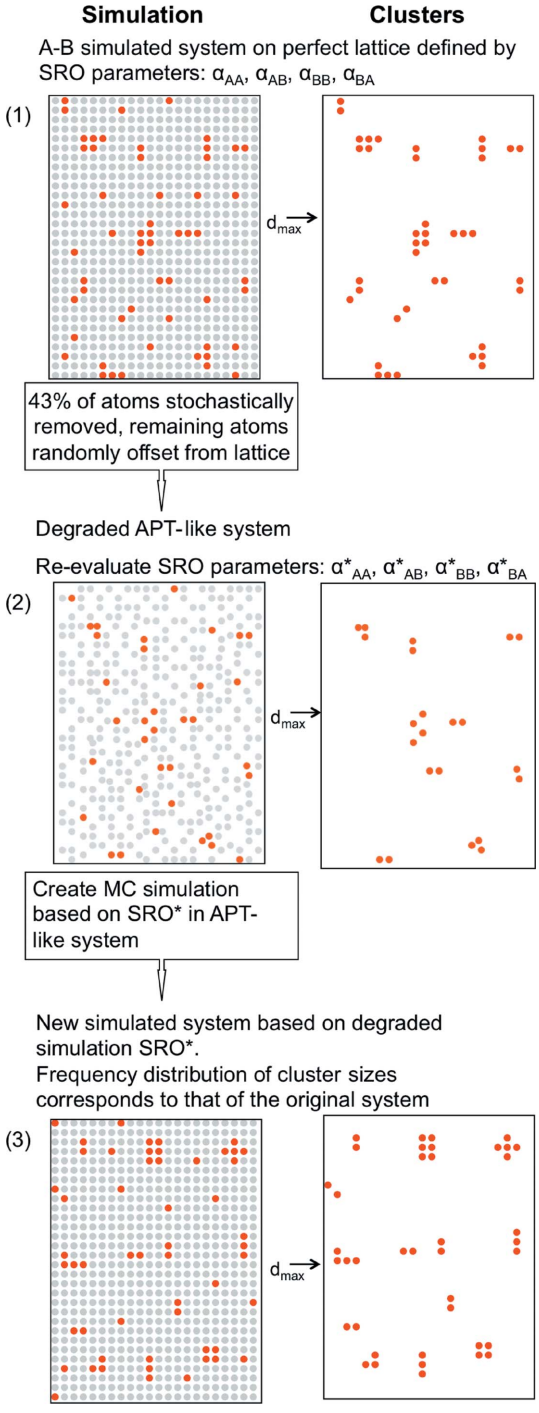


**Figure 7**
Flow chart of the first simulation test. This test first creates a simulation with certain GM-SRO. Degradation to an APT-like system is performed, and the GM-SRO is measured in this degraded system. A new simulation is then performed, using the measured GM-SRO from the degraded system.

## 4. Results and analysis

### 4.1. GM-SRO analysis of experimental APT data

The complete set of possible GM-SRO parameters was characterized up to the 12th crystallographic shell ($m$ = 12) in each reconstruction, which corresponds to less than a 1 nm radius from the central reference atom. Fig. 8 provides the matrix of all possible first-shell ($m$ = 1) solute–solute GM-SRO correlations for each of the thermal treatments studied. The as-quenched (AQ) condition for the first shell shows very small magnitudes of GM-SRO overall, some even negative, indicating minimal segregation in the first shell. The 60 s case exhibits uniformly larger values of GM-SRO and has the largest GM-SRO magnitude for $\alpha^{m=1}_{\{CuMg\}\{Cu\}}$. Fig. 8 also demonstrates similarly ranged values of GM-SRO for the data from the sample aged for 1 h at 423 K.

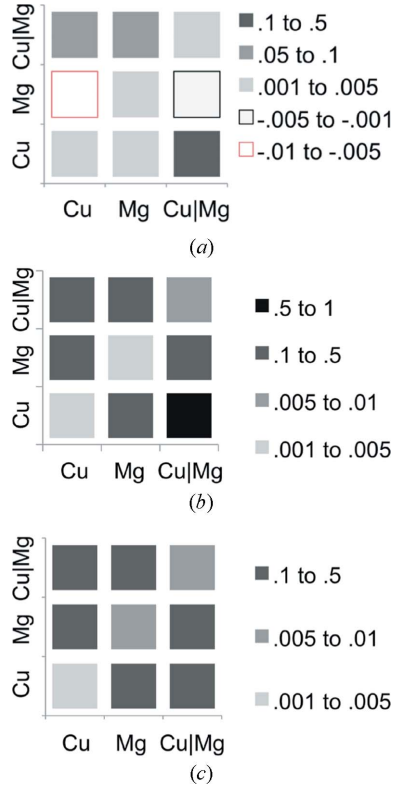


**Figure 8**
Matrix of first-shell GM-SRO value results for an Al–1.1 Cu–1.7 Mg (at.%) alloy that has been aged at 423 K for (*a*) 0 s (AQ), (*b*) 60 s and (*c*) 1 h. The light-red outlined squares indicate a negative SRO, whereas the grey squares show varying levels of solute clustering (lighter squares depict the lower significance values, and darker squares indicate the higher significance values).

The results presented in Fig. 8 are constrained to the first-shell solute–solute correlations. However, in each case, the total GM-SRO information (obtained from each APT data set) provides the average radial dependence of solute distribution around each atom for up to the 12th crystallographic shell. The increased GM-SRO at higher radii is not necessarily straightforward to interpret; however it likely indicates the presence of increasingly large isotropic clusters containing both solutes.

### 4.2. Solute cluster analysis of experimental APT data

The 3DMF clustering algorithm was applied to each of the APT reconstructions, with $d_{max}$ = 0.35 nm. In each case, the cluster-size frequency distribution was initially characterized with respect to clusters containing either or both Cu and Mg atoms (*i.e.* Cu and Mg atoms were convoluted and solute clusters were characterized as pseudo-binary systems, where pseudo-binary refers to the solute atoms being considered as a

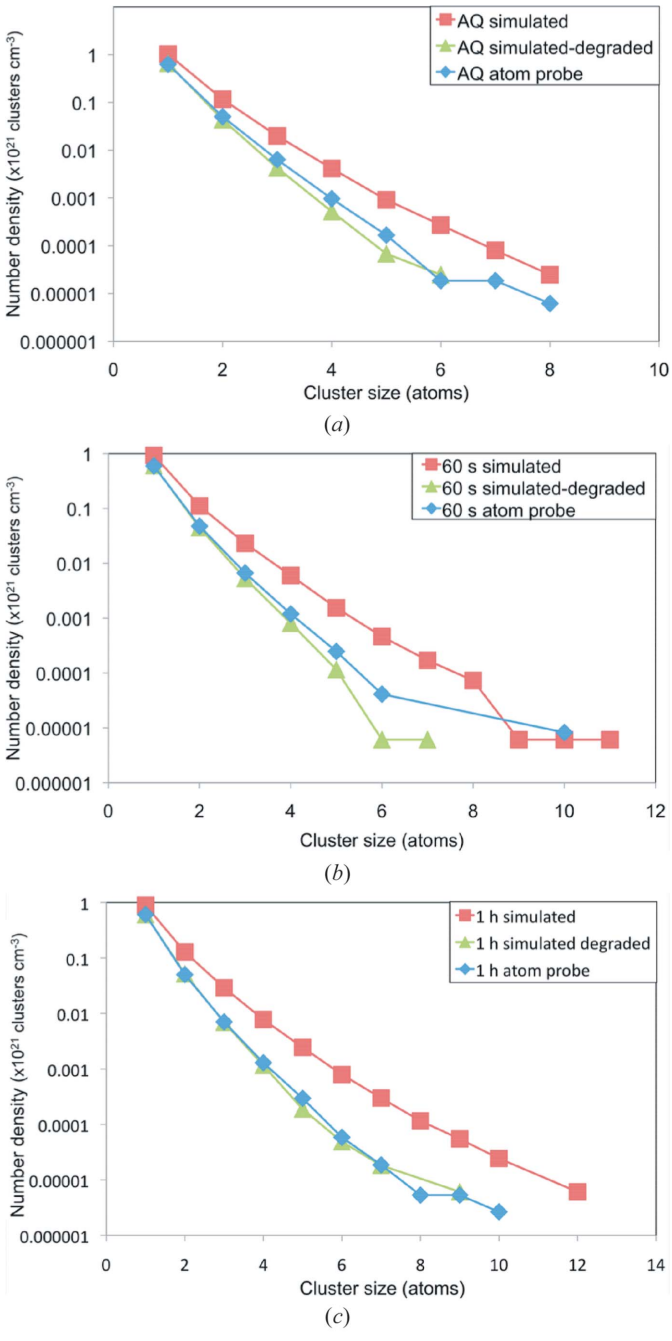


**Figure 9**
Cluster-size distributions for the simulated (simulated), simulated with model detector efficiency (simulated-degraded) and original atom-probe (atom probe) data sets. Ageing conditions of Al–1.1 Cu–1.7 Mg (at.%) presented are (*a*) AQ, (*b*) 60 s and (*c*) 1 h.

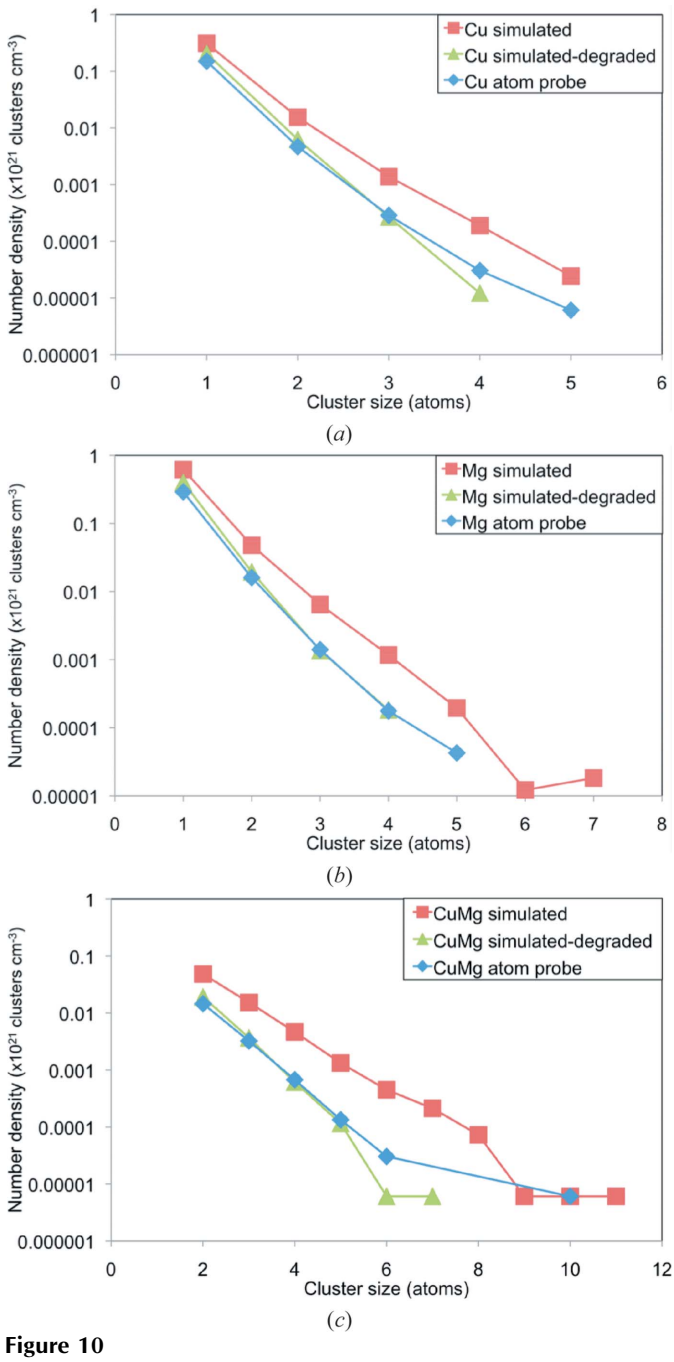


**Figure 10**
Cluster-size distributions for the simulated (simulated), simulated with model detector efficiency (simulated-degraded) and original atom-probe (atom probe) data sets, for the 60 s aged condition of Al–1.1 Cu–1.7 Mg (at.%). (*a*) Pure Cu clusters, (*b*) pure Mg clusters and (*c*) clusters containing both Cu and Mg atoms.

single species rather than separately). The results are shown in Fig. 9. The analysis was then repeated for the characterization of pure Cu clusters (*i.e.* Mg was ignored and only Cu atoms within $d_{max}$ of another Cu atom were deemed clustered), pure Mg clusters, and clusters simultaneously containing at least one Cu and at least one Mg atom. The resulting cluster-size frequency distributions for the APT reconstruction corresponding to 60 s ageing are presented in Fig. 10.

### 4.3. MC simulations targeting APT-derived GM-SRO

The described GM-SRO-targeted MC simulations were implemented to create complete lattice-based systems of $10^7$ atoms based upon the respective experimental measurements. Simulation of the AQ condition utilized the $\{\alpha^m_{CuCu}, \alpha^m_{CuMg}, \alpha^m_{MgCu}, \alpha^m_{MgMg}\}^{12}_{m=1}$ subset of GM-SRO parameters. For simulation of the 60 s aged condition the $\{\alpha^m_{CuCu}, \alpha^m_{CuMg}, \alpha^m_{MgCu}, \alpha^m_{MgMg}, \alpha^m_{AlCu}, \alpha^m_{AlMg}\}^{4}_{m=1}$ subset of GM-SRO parameters were used. Finally, the 1 h aged case was simulated using the GM-SRO subset of $\{\alpha^m_{CuCu}, \alpha^m_{CuMg}, \alpha^m_{MgCu}, \alpha^m_{MgMg}, \alpha^m_{AlCu}, \alpha^m_{AlMg}\}^{5}_{m=1}$.

The complete set of experimentally derived GM-SRO parameters was not utilized in any of these cases due to the fact that APT data are imperfect. Take the example of a particular lattice site adjacent to a Cu atom in a complete lattice-based Al–Cu–Mg system. It can be assumed that measurement of site-occupancy probabilities in this system would show that the sum of the probabilities that this site contains an Al, Mg or Cu atom is equal to unity. However, site-occupancy measurements derived from APT data with 57% detection efficiency and imperfect spatial resolution cause this assumption to fail. Therefore, only GM-SRO values with the solute elements as the nearest neighbour are used in the MC simulation.

The 3DMF clustering algorithm was then applied to each of the APT reconstructions, with $d_{max}$ = 0.35 nm to each of the simulations, and the results are plotted in comparison to the results from the corresponding original APT reconstructions in Figs. 9 and 10. Significantly, these cluster-size frequency distributions should be representative of the distribution existing in the original specimen.

### 4.4. Effect of data quality

In the final step of this analysis, as a check of self-consistency, the simulated data are artificially deteriorated to approximate how an APT analysis would render this theoretical system and the solute clustering analysis is repeated. That is, a complete perfect lattice system has been simulated based upon GM-SRO measurements of APT reconstructions. If the effects of limited detection efficiency and spatial resolution are imposed upon these simulations, then the resulting atomic distribution should be statistically equivalent to the original APT reconstruction on which it is based. In this analysis this equivalence is tested by examination of the cluster-size frequency distributions. This procedure is summarized in the flow chart provided in Fig. 11.

Hence, the effects of finite detector efficiency, simulated by the stochastic removal of 43% of atoms, and limited spatial resolution, based on a Gaussian blurring of the atomic coordinates, were modelled in the simulated data sets. Subsequently the 3DMF cluster identification algorithm was applied, the results of which are shown in comparison to both the corresponding APT reconstruction and the original complete reconstruction in Figs. 9 and 10. In each case, the

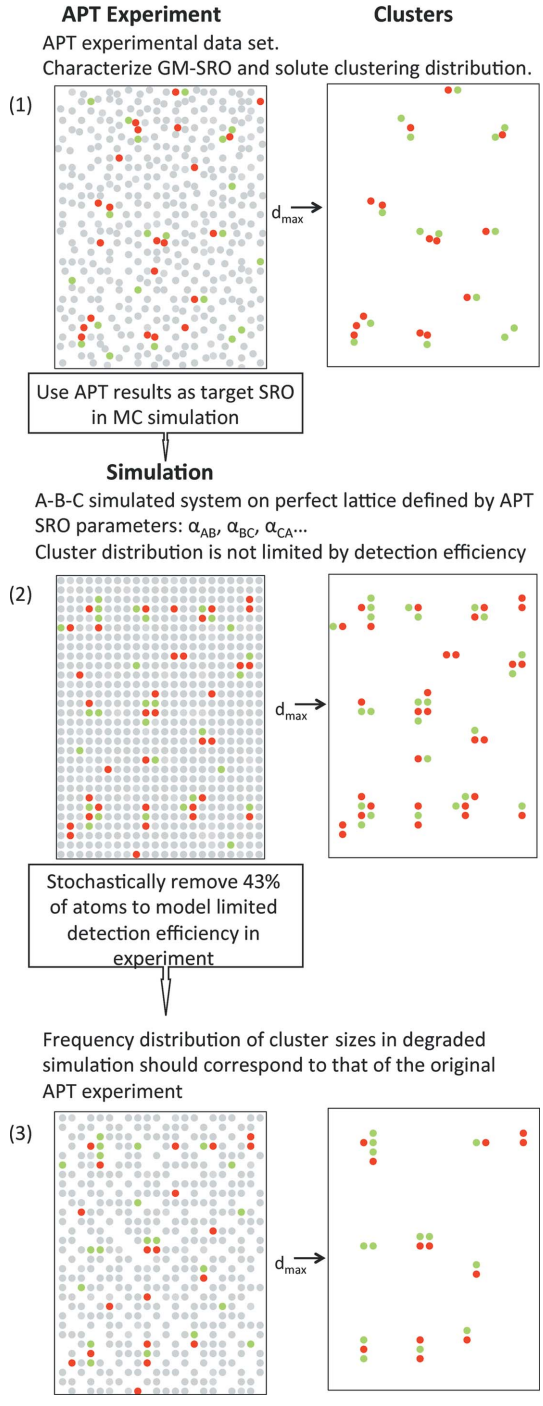


**Figure 11**
Flow chart of the second simulation test. First the GM-SRO is measured in an APT data set. This GM-SRO is used as the target in a new MC simulation, and the resulting data set is degraded to an APT-like degree.

resulting cluster-size frequency distribution converges closely to the experimental distribution measured from APT experiments, indicating the procedures are self-consistent. This is strong and internally consistent evidence that based on the analysis of GM-SRO in APT reconstructions it is possible to retrieve a highly accurate picture of the distribution of atoms on the lattice in the original specimen.

## 5. Discussion

Fig. 6 reveals the quantitative nature of the relationship between the GM-SRO parameters and the cluster-size distributions. In terms of the general trends, the results are as might be expected, since the GM-SRO is based upon site-occupation probabilities. Hence, at higher values of GM-SRO, the solute pairs are more likely to be local neighbours; thus there are increased probabilities that larger solute clusters can occur. Although the present results demonstrate that atom-probe measurements of GM-SRO can reproduce the cluster-size frequency distribution in an equivalent simulation, it must be pointed out that the two solid solutions are not identical in terms of the precise setting of individual atoms in the lattice. Certainly, the MC approaches described here do not converge to a unique atomic configuration. However, they do generate an atomistic simulated system that is statistically equivalent, in terms of the distribution of solute atoms in shell neighbourhoods. The more GM-SRO information that is available from the original system for input into the simulation, the greater the capacity to capture higher-order subtleties and nuance in the simulated atomic distributions.

A promising result comes *via* the investigation of the effects of detector efficiency on GM-SRO measurements, as demonstrated in Fig. 4. Limitations in detector efficiency can reduce the viability of a range of data-mining approaches that were developed for the characterization of solute distributions within APT data. In many cases, the effect of limited detector efficiency can introduce a bias where the atoms seem more randomly distributed, as recently demonstrated for the case of a voxel-based frequency distribution analysis (Moody *et al.*, 2008). Significant effects, due to the detector, have also been found in nearest-neighbour analyses (Stephenson *et al.*, 2007). However, as is most relevant to this study, detection efficiency has been shown to significantly influence the characterization of fine-scale clusters *via* APT (Stephenson *et al.*, 2011). The results of such experimental limitations on the characterized cluster density are perhaps most effectively conveyed *via* the small sub-volumes in Fig. 12. The GM-SRO approach described here is significant in that it provides a means for a thorough characterization of APT data that is, between certain limits, independent of detection efficiency (Fig. 8). The limits are affected by the system size, solute concentration and detection efficiency.

Previously, de Geuser *et al.* (2006) developed and applied a pair-correlation function approach to investigate the onset and evolution of solute SRO in the APT study of a thermally treated Al–Mg–Si alloy. The pair-correlation function is closely related to the GM-SRO parameter. However, unlike the GM-SRO approach applied in this study, the pair-correlation function does not consider the structures within and between the atomic shells existing in the crystal lattice. This is significant because the APT technique has the capacity to generate atomistic data from a system that includes significant information about the nearest-neighbour distributions. One important precaution in using the GM-SRO analyses relates to systems that contain large second-phase precipitates. These precipitates may cause significantly different electric-field intensities in order to achieve field evaporation. Such systems are prone to severely degraded resolution of solute-enriched neighbourhoods. This degradation is caused by large ion trajectory aberrations in the original experiment due to local magnification effects. In these systems elements may be preferentially evaporated in between pulses by the DC voltage. These atoms are lost to the analysis, leading to the depletion of particular elements and nullification of the assumption that the detection efficiency of the APT experiment is a purely stochastic process. In such a case, application of SRO analyses may provide unrealistic results. These issues can be managed by either careful operation of the atom probe to ensure uniform evaporation, or the discrimination of the data, so as to operate only on regions that are precipitate free.

The main advantage of using the Monte Carlo simulation approach (Fig. 2) is the capacity to determine the chemical configuration of an atomic scale system with given experimental GM-SRO parameters, without the need to use thermodynamic data such as interaction potentials. Against this, however, is the fact that the calculation of the simulated data set to match the APT data was, at times, quite challenging. Attempts to simultaneously converge a set of GM-SRO parameters to their target values, defined across multiple crystallographic shells, were sometimes problematic. For example, as the algorithm progresses, it can become more difficult to find a suitable pair of atoms that could swap, despite the large number of atoms, that would reduce the overall residual. Instead, the algorithm at first only considered the first-shell ($m$ = 1) GM-SRO values. After reaching the target convergence criteria for the first shell, the second shell ($m$ = 2) GM-SRO values were examined. In this way, higher-order shell SRO values were consecutively considered until convergence was not possible. This allowed the algorithm to run freely and unsupervised, and ensured maximum information extraction from the system under investigation.

In Fig. 9, all three pseudo-binary Cu–Mg cluster-size distribution graphs for the AQ, 60 s and 1 h cases show good agreement between the original APT data and the simulated data with efficiency of 57% and spatial blurring with an ellipsoidal Gaussian. It is highly encouraging that the significant complexity within APT data can be closely reproduced based simply on using the measured GM-SRO values to generate a simulated atomistic system. Furthermore, Fig. 10 demonstrates that the MC simulations can reproduce the intricacy of the solute distribution beyond that of a simple binary system. The Cu–Cu, Mg and Mg–Cu correlations in the 60 s case have each been well described *via* GM-SRO para-

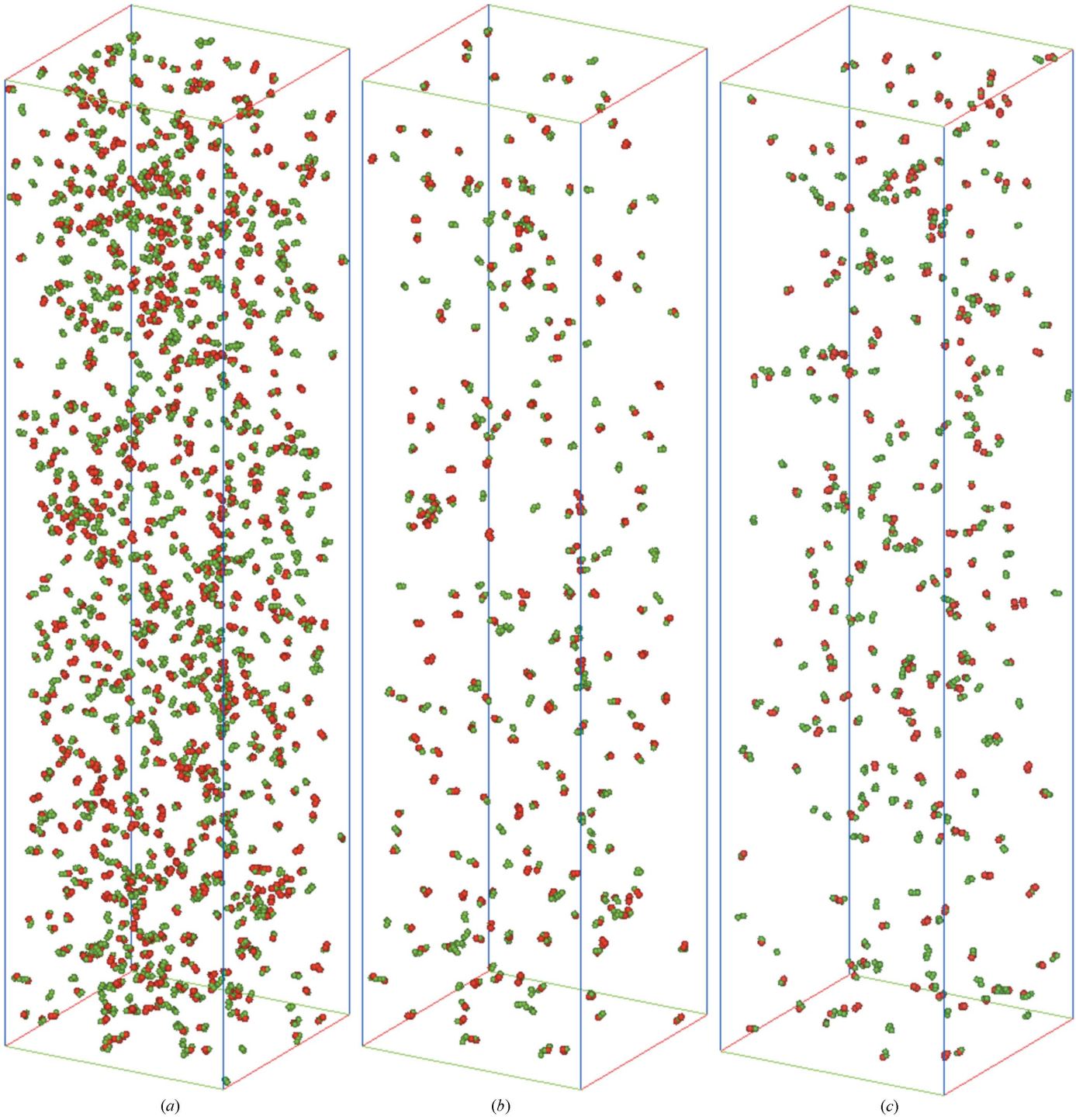


**Figure 12**
Atom map of solute clusters identified within 20 × 20 × 100 $nm^3$ sub-volumes of APT experimental data and associated MC simulations (using the first four shells, and using GM-SRO parameters that do not have aluminium as the nearest-neighbour element) corresponding to the frequency distributions in Fig. 10(*b*). (*a*) Clusters in the complete simulated system based on GM-SRO characterization of Al–1.1 Cu–1.7 Mg, 60 s aged condition, (*b*) clusters identified in the MC simulation after the stochastic removal of atoms to model 57% detector efficiency of APT, (*c*) cluster characterization within the original APT reconstruction of Al–1.1 Cu–1.7 Mg, 60 s aged condition.

meters, and the close match of the cluster-size distribution between the experimentally measured and the degraded simulated system indicates that the complex solute architecture in the original specimen has been accurately reproduced.

The ability to simulate the original atomic distribution using APT-based GM-SRO parameters and thereby estimate actual cluster-size frequency distributions is a significant outcome of this research. Such quantitative information is invaluable for a range of materials research investigations. Previously,

Stephenson *et al.* (2011) derived an analytical deconvolution method to calculate the original physical distribution of solutes from an APT detection-efficiency-degraded distribution, providing the means to back-calculate the 'actual' number densities of clusters from atom-probe results. This approach is a more straightforward computation; however, it only outputs the cluster-size frequency distribution. Alternatively, the GM-SRO-based MC simulations create large and complete atomistic systems, within which the solute architecture may be interrogated directly using a range of analysis methods. Significantly, it facilitates experimentally derived three-dimensional atomic structures to assess the quality of atomistic models and simulations and, further, to be seeded directly into them. This represents an indispensable tool for furthering understanding of key correlations and fundamental atomic relationships driving macroscopic properties.

## 6. Conclusions

The GM-SRO is a powerful measure of solute distributions in a multicomponent solid solution. In this study the GM-SRO definition has been adapted to characterize solute distributions in imperfect APT data. Simulations have demonstrated that, provided the data are of a high quality, then with sufficient statistics (*i.e.* the size of the reconstructed volume) the SRO parameters measured within APT reconstructions can be highly representative of the atomic arrangement in the actual system. The significance of the influence of detection efficiency depends on the size of the data set, and the concentration of the relevant solute within the material. The capacity of APT to measure the three-dimensional arrangement of atoms at the nanoscale in multicomponent systems combined with the generalized multicomponent SRO parameter to interpret this information represents a significant advance to crystallography.

It has been demonstrated that the GM-SRO is directly related to the cluster-size frequency distribution of solutes within the system. The GM-SRO technique has been applied to real experimental data from a ternary Al–Cu–Mg alloy. It was shown that the GM-SRO measurements provide a new means of classifying structural correlations, which are robust in the presence of limited detector efficiency. Based upon target GM-SRO values derived from APT data, MC-based atomistic simulations have been used to generate a corresponding system with an atomic configuration that is statistically equivalent to that from the original specimen. The way in which an APT experiment would visualize these perfect systems can be modelled by artificially imposing the limitations of experiments on the simulation. It is demonstrated that the simulated APT-like systems correspond closely to the original APT experimental reconstructions. This is strongly indicative of the accuracy of the APT-measured SRO and the capacity to use this information to simulate realistic representation of the atomic arrangements in the original system.

The combination of APT-based GM-SRO measurements and Monte Carlo simulations is a valuable new tool in the field of crystallography and characterization. It represents a step further into the realm of the crystallography of entire systems of chemically complex, multicomponent solid solutions.

The authors are grateful for the scientific and technical input and support from staff at the University of Sydney node of the Australian Microscopy and Microanalysis Research Facility (AMMRF), in particular Drs Leigh Stephenson, Baptiste Gault and Daniel Haley. AVC is grateful for an Australian Postgraduate Award and a CSIRO top-up scholarship. Part of this research was undertaken on the NCI National Facility in Canberra, Australia, which is supported by the Australian Government.

## References

Bas, P., Bostel, A., Deconihout, B. & Blavette, D. (1995). *Appl. Surf. Sci.* **87**, 298–304.
Bentley, J. L. (1975). *Commun. ACM*, **18**, 509–517.
Cadel, E., Vurpillot, F., Larde, R., Duguay, S. & Deconihout, B. (2009). *J. Appl. Phys.* **106**, 044908.
Castell, M. R., Muller, D. A. & Voyles, P. M. (2003). *Nat. Mater.* **2**, 129–131.
Ceguerra, A. V., Moody, M. P., Stephenson, L. T., Marceau, R. K. W. & Ringer, S. P. (2010). *Philos. Mag.* **90**, 1657–1683.
Ceguerra, A. V., Powles, R. C., Moody, M. P. & Ringer, S. P. (2010). *Phys. Rev. B*, **82**, 132201.
Clouet, E., Laé, L., Epicier, T., Lefebvre, W., Nastar, M. & Deschamps, A. (2006). *Nat. Mater.* **5**, 482–488.
Cockayne, D. J. H. & McKenzie, D. R. (1988). *Acta Cryst.* A**44**, 870–878.
Cowley, J. M. (1950*a*). *J. Appl. Phys.* **21**, 24–30.
Cowley, J. M. (1950*b*). *Phys. Rev.* **77**, 669–675.
Cowley, J. M. (1960). *Phys. Rev.* **120**, 1648–1657.
Cowley, J. M. (1968). *Acta Cryst.* A**24**, 557–563.
Cowley, J. M. (1995). *Diffraction Physics*, 3rd ed. Amsterdam: North Holland.
Cowley, J. M. & Murray, R. J. (1968). *Acta Cryst.* A**24**, 329–336.
Fontaine, D. de (1971). *J. Appl. Cryst.* **4**, 15–19.
Gault, B., Haley, D., de Geuser, F., Moody, M. P., Marquis, E. A., Larson, D. J. & Geiser, B. P. (2011). *Ultramicroscopy*, **111**, 448–457.
Gault, B., La Fontaine, A., Moody, M. P., Ringer, S. P. & Marquis, E. A. (2010). *Ultramicroscopy*, **110**, 1215–1222.
Gault, B., Moody, M. P., de Geuser, F., Haley, D., Stephenson, L. T. & Ringer, S. P. (2009). *Appl. Phys. Lett.* **95**, 034103.
Gault, B., Moody, M. P., De Geuser, F., La Fontaine, A., Stephenson, L. T., Haley, D. & Ringer, S. P. (2010). *Microsc. Microanal.* **16**, 99–110.
Gehlen, P. C. & Cohen, J. B. (1965). *Phys. Rev.* **139**, A844–A855.
Geiser, B. P., Kelly, T. F., Larson, D. J., Schneir, J. & Roberts, J. P. (2007). *Microsc. Microanal.* **13**, 437–447.
Gerold, V. & Kern, J. (1987). *Acta Metall.* **35**, 393–399.
Geuser, F. de, Lefebvre, W. & Blavette, D. (2006). *Philos. Mag. Lett.* **86**, 227–234.
Haley, D., Petersen, T., Barton, G. & Ringer, S. P. (2009). *Philos. Mag.* **89**, 925–943.
Heinrich, A., Al-Kassab, T. & Kirchheim, R. (2003). *Mater. Sci. Eng. A*, **353**, 92–98.
Hyde, J. M. & English, C. A. (2000). *Symposium R: Microstructural Processes in Irradiated Materials*. *Mater. Res. Soc. Symp. Proc.* Vol. 650, pp. R6.6.1–R6.6.12. Boston: MRS.
Kelly, T. F. & Miller, M. K. (2007). *Rev. Sci. Instrum.* **78**, 031101.
McGreevy, R. L. & Pusztai, L. (1988). *Mol. Simul.* **1**, 359–367.
Marceau, R. K. W., Sha, G., Ferragut, R., Dupasquier, A. & Ringer, S. P. (2010). *Acta Mater.* **58**, 4923–4939.
Mellergård, A. & McGreevy, R. L. (1999). *Acta Cryst.* A**55**, 783–789.

Miller, M. K. (2000). *Atom Probe Tomography: Analysis at the Atomic Level.* New York: Springer.
Miller, M. K. & Kenik, E. A. (2004). *Microsc. Microanal.* **10**, 336–341.
Moody, M. P., Gault, B., Stephenson, L. T., Haley, D. & Ringer, S. P. (2009). *Ultramicroscopy*, **7**, 815–824.
Moody, M. P., Stephenson, L. T., Ceguerra, A. V. & Ringer, S. P. (2008). *Microsc. Res. Tech.* **71**, 542–550.
Newman, M. E. J. & Barkema, G. T. (1999). *Monte Carlo Methods in Statistical Physics.* India: Clarendon Press.
Nie, J., Muddle, B., Aaronson, H., Ringer, S. & Hirth, J. (2002). *Metall. Mater. Trans. A*, **33**, 1649–1658.
Nield, V. M., Keen, D. A., Hayes, W. & McGreevy, R. L. (1992). *J. Phys. Condens. Matter*, **4**, 6703–6714.
Nield, V. M., Keen, D. A. & McGreevy, R. L. (1995). *Acta Cryst.* A**51**, 763–771.
Pereloma, E. V., Shekhter, A., Miller, M. K. & Ringer, S. P. (2004). *Acta Mater.* **52**, 5589–5602.
Proffen, Th. & Welberry, T. R. (1997). *Acta Cryst.* A**53**, 202–216.
Proffen, Th. & Welberry, T. R. (1998). *J. Appl. Cryst.* **31**, 318–326.
Ralston, K. D., Birbilis, N., Cavanaugh, M. K., Weyland, M., Muddle, B. C. & Marceau, R. K. W. (2010). *Electrochim. Acta*, **55**, 7834–7842.
Ringer, S. P. & Hono, K. (2000). *Mater. Charact.* **44**, 101–131.
Seidman, D. N. (2007). *Annu. Rev. Mater. Res.* **37**, 127–158.
Stephenson, L. T., Moody, M. P., Gault, B. & Ringer, S. P. (2011). *Microsc. Res. Tech.* **74**, 799–803.
Stephenson, L. T., Moody, M. P., Liddicoat, P. V. & Ringer, S. P. (2007). *Microsc. Microanal.* **13**, 448–463.
Tucker, M. G., Dove, M. T. & Keen, D. A. (2001). *J. Appl. Cryst.* **34**, 630–638.
Vaumousse, D., Cerezo, A. & Warren, P. J. (2003). *Ultramicroscopy*, **95**, 215–221.
Vurpillot, F., de Geuser, F., Da Costa, G. & Blavette, D. (2004). *J. Microsc. (Oxford)*, **216**, 234–240.
Welberry, T. R. (1985). *Rep. Prog. Phys.* **48**, 1543–1594.
Welberry, T. R. & Proffen, Th. (1998). *J. Appl. Cryst.* **31**, 309–317.
Zhu, A., Gable, B. M., Shiflet, G. J. & Starke, E. A. Jr (2004). *Acta Mater.* **52**, 3671–3679.